PHYSICAL REVIEW B **77**, 075406 (2008)

Growth, atomic structure, and vibrational properties of MnO ultrathin films on Pt(111)

Ch. Hagendorf,* S. Sachert, B. Bochmann, K. Kostov,† and W. Widdra‡
Institute of Physics, Martin-Luther-Universität Halle-Wittenberg, 06099 Halle, Germany

(Received 2 May 2007; published 7 February 2008)

Ultrathin films of MnO have been grown by reactive metal deposition in an O_2 atmosphere on Pt(111) and studied using scanning tunneling microscopy (STM), low-energy electron diffraction, temperature programmed desorption, and high-resolution electron energy loss spectroscopy. *In situ* STM experiments which have been performed during film growth at elevated temperatures show that MnO grows highly ordered in a layerlike mode on Pt(111). The first MnO monolayer exhibits large, uniaxial reconstructed domains with a (19×1) periodicity, which results in rotational domains on the hexagonal Pt(111) substrate. Growth and structural properties of the (19×1) reconstruction are discussed in a model based on long-range ordering of antiphase boundaries within a uniaxially reconstructed and otherwise bulklike MnO(001) monolayer. The vibrational spectra for the MnO monolayer are dominated by a strong and narrow surface phonon peak at 368 cm^{-1}, which is identified as the out-of-plane vibration of the O sublattice against the Mn sublattice based on the ^{16}O to ^{18}O isotope shift. After completion of the MnO monolayer, multilayer growth mode is found at higher coverages (>1.5 ML). The appearance of the second MnO layer is accompanied by an additional Fuchs-Kliewer phonon mode at 545 cm^{-1}.

DOI: 10.1103/PhysRevB.77.075406 PACS number(s): 68.47.Gh, 68.37.Ef, 63.22.−m, 68.55.A−

I. INTRODUCTION

The particular electronic and magnetic properties of 3*d* transition metal oxides have raised an increased scientific and technological interest over the past years. Manganese oxides are technologically interesting as electrode material,[1] for magnetic applications,[2] and in heterogeneous catalysis.[3] Beyond these applications, the scientific interest has focused on the special electronic properties of 3*d* transition metal monoxides like CoO, NiO, and MnO.[4,5] In recent investigations of MnO, it has been shown that the variety of structural, electronic, and magnetic properties are strongly interdependent.[6] Additionally, several unusual magnetic and electronic properties have been observed for MnO ultrathin films and nanoparticles which are related to their reduced size, stoichiometry, and the presence of defects.[7,8] A profound investigation of nucleation and growth mechanism is crucial for understanding, controlling, and implementing size-dependent and defect-induced properties of MnO ultrathin films or nanoparticles.

Among several stable manganese oxide phases with different stoichiometries and structures, MnO is dominating at low O_2 partial pressure.[9] The properties of bulk MnO are well understood.[10] MnO is electrically insulating, antiferromagnetic, and has rocksalt structure. In contrast, relatively little is known about the surface properties of a MnO solid due to its insulating nature and difficulties in surface preparation.[5] Referring to the rocksalt structure, a nonpolar (001) and a polar (111) bulklike surface termination are expected.[11] Only recently, the structural and electronic features of resulting MnO(111) and MnO(100) reconstructions have been studied theoretically.[12,13]

The difficulties occurring in experimental studies of bulk MnO surfaces could be circumvented by the deposition of thin oxide layers on conducting substrates.[14] With the use of different deposition methods including metal organic chemical vapor deposition,[15] pulsed laser deposition,[16] and reactive deposition,[14] it has been shown that MnO layers can be grown epitaxially. Reactive deposition by thermal evaporation of metal atoms in an O_2 atmosphere has proven to be a suitable method for growing atomically perfect epitaxial layers of many transition metal oxides on metal substrates.[17] The quality of the obtained oxide layers is essentially determined by the lattice mismatch, orientation, thermal stability, and O reactivity of the substrate. In the case of MnO on Ag(001), epitaxial layers have been successfully prepared by Müller *et al.*[14] despite a large lattice mismatch of 9% [$a_{\mathrm{MnO}}=0.444$ nm and $a_{\mathrm{Ag}}=0.409$ nm (Ref. 18)]. For MnO on Pt(111), the lattice mismatch of 13.3% [$a_{\mathrm{Pt}}=0.392$ nm (Ref. 18)] is even larger. However, thin film quality may be improved due to a higher thermal stability of the Pt compared to the Ag substrate during annealing steps. Furthermore, the hexagonal symmetry of the Pt(111) substrate may induce the formation of (111)-oriented oxide films as was found for ZrO_2/Pt(111).[19,20]

In this work, we show that a well-ordered (100)-like MnO phase grows on the hexagonal Pt(111) substrate. The resulting (19×1) morphology and the atomic structure of the first MnO monolayer as well as the vibrational properties will be discussed.

II. EXPERIMENT

The experiments were performed in two ultrahigh vacuum (UHV) chambers at base pressures below 3×10^{-10} mbar. One UHV system is equipped with a variable-temperature scanning tunneling microscope (Omicron VT-AFM/STM, Germany) which allows *in situ* Mn deposition from an electron beam heated source during scanning tunneling microscopy (STM) imaging at elevated temperatures (400–550 K). Via a capillary array doser, a molecular beam of O_2 can be directed onto the sample in the STM at a locally increased partial pressure. The second UHV system houses a spectrometer for high-resolution electron energy loss spectroscopy

(HREELS; Delta 05, VSI, Germany) and thermal desorption spectroscopy (TPD) facilities as described elsewhere.[21] Standard surface science methods for sample cleaning (Ar^+ sputtering and heating), analysis of surface composition (Auger electron spectroscopy), and long-range ordering (low-energy electron diffraction, LEED) are available in both systems.

The Pt(111) surface was cleaned by Ar^+ sputtering at room temperature, and subsequent cycles of sputtering at 1000 K and flashing at 1250 K. Depending on the amount of MnO deposited during film growth, several preparation cycles were necessary to clean the Pt(111) surface. STM images of the clean surface show smooth terraces with straight step edges, free of adsorbates and impurities due to Mn segregation.

Thin film growth experiments were performed by Mn deposition in an O_2 atmosphere of 2×10^{-7} mbar. An estimate of the deposition rate was achieved from series of STM images during deposition of layerlike growing MnO films on Pt(111). Alternatively, CO titration experiments were used in the submonolayer regime as will be discussed below. Low deposition rates (1 ML/h) were applied to allow STM imaging during the film growth. The Mn deposition rate was monitored and controlled by the flux of Mn ions present in the evaporated Mn beam. With the aid of a capillary gas doser, an O_2 partial pressure is obtained in front of the sample mounted in the STM, which is increased by a factor of about 10 with respect to the background pressure in the UHV chamber. Thus, an ion getter pump could be used for pumping the background gas phase. Compared to previous experiments applying a turbo molecular pump or static O_2 backfilling of the UHV system,[22] this method improved the chemical and mechanical stability of the STM during high-resolution measurements. An estimate of the pressure gradient was obtained by STM *in situ* measurements of the Pt(111)-(2×2)-O structure at 300 K, which is known to develop after dosing of 2000 L ($1\ \mathrm{L} = 10^{-6}$ Torr s) molecular oxygen.[23] This value was compared to the measured pressure and deposition time.

The influence of the tunneling tip on the *in situ* Mn-O deposition experiments was investigated by shifting the lateral imaging positions by several 100 nm during imaging. Any influence on the growth mode could not be observed. Depending on the tip apex ratio, the Mn coverage increases outside of the scanning region due to the tip shadow in the Mn beam. This effect could be reduced by choosing a sharp tip (tip radius <50 nm) and a large imaging area (400 nm) during deposition. A shadowing effect regarding the access of oxygen to the tip sample region has not been observed.

For TPD experiments, the quadrupole mass spectrometer (Balzers QMG 112) is equipped with a Feulner cup and a constant heating rate of 2 K/s was used. All HREEL spectra were recorded at 80 K with an electron energy of 4 eV. If not stated otherwise, the experiments have been performed in specular reflecting geometry with a total of 120° scattering angle. Depending on the details of the experiments, overall experimental energy resolutions between 9 and 24 cm^{-1} were used.

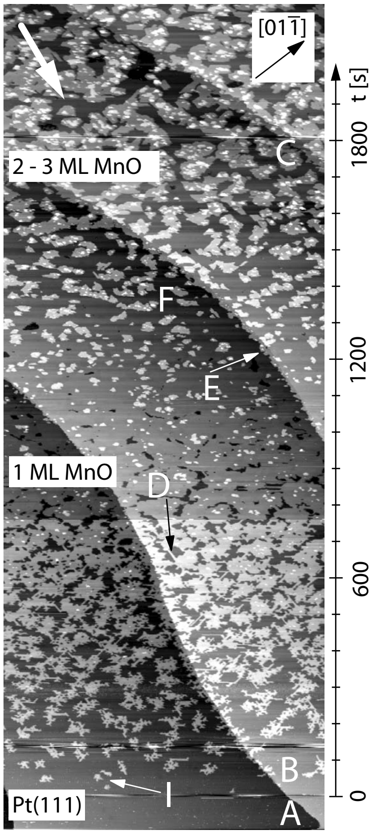

FIG. 1. STM image *during* deposition of MnO on Pt(111) at 400 K in an O_2 atmosphere of 2×10^{-7} mbar. A total amount of 2–3 ML MnO is deposited at a rate of 3 ML/h incident from the top left corner (arrow). Deposition was started at the lower part of the image ($t = 0$ s) and continued while scanning over a time interval of 2500 s. The STM overview image is composed of three scans. From bottom to top, the scans have been shifted by the width of the quadratic imaging area after each measurement ($400 \times 1200\ \mathrm{nm}^2$, $U = -3.5$ V, $I = 0.03$ nA, and $T_{\mathrm{sample}} = 400$ K).

III. RESULTS

A. Growth

MnO films were grown on Pt(111) at a temperature of 400 K by deposition of Mn in O_2 atmosphere of 2×10^{-7} mbar. These values were chosen with reference to a study by Müller *et al.*,[14] where epitaxial MnO films on Ag(001) could be obtained at similar growth conditions. A large *in situ* STM overview recorded during deposition of Mn in O_2 atmosphere at elevated temperatures is shown in Fig. 1. The image is composed of three STM measurements subsequently acquired over a time interval of 1 h. Each of the images covers an area of $400 \times 400\ \mathrm{nm}^2$ and has been shifted by 400 nm from bottom to top after the measurement. Since the Mn atoms hit the surface at grazing incidence from the top direction (arrow in Fig. 1), a shadowing effect of the tunneling tip is reduced by repeatedly shifting the imaging area against the direction of the atomic beam. MnO deposition is started on the clean Pt(111) surface visible in the lower part of Fig. 1. The opening of the evaporator shutter can clearly be distinguished in the measurement and marks

$t=0$ s (right axis in Fig. 1) due to mechanical oscillations induced by manual operation of the shutter (A). The oscillations at about 140 s are related to an O_2 pressure adjustment during the measurement (B). Deposition is performed over a time interval of 1800 s until the shutter is closed (at position C).

Nucleation of the first monolayer occurs on top of the substrate terraces within the first 60 s after opening the shutter. The average nucleation density is in the range of $1/250\ \text{mm}^2$ on the terraces for the given surface temperature of 400 K. Additionally, a decoration of the upper and the lower side of substrate step edges is observed. After nucleation, the islands (marked I) continue to grow by capturing diffusing atoms. A diffusion length larger than 50 nm inhibits further nucleation on the substrate and on top of the islands during the growth of the first half monolayer. The islands of the first monolayer are irregularly shaped with branches extending into the three equivalent $[01-1]$ directions of the substrate. The branches appear mostly with a fractal-dendritic contour. However, at some locations (marked D, 700 s), one-dimensional extensions in $[01-1]$ direction are observed with a width of 1–2 nm and a length of up to 20 nm. At slightly higher growth temperatures (450–500 K, not shown here), more compact islands are obtained. Also, subsequent annealing of submonolayer coverages at 400 K in UHV without further material deposition leads to less frizzy step edges and more compact islands.

At a coverage of 0.8 ML after approximately 700 s, nucleation in the second monolayer sets in. The islands are preferentially located in the central part of larger islands of the first monolayer. The increased nucleation density of $1/100\ \text{nm}^2$ (700–1000 s) may be related either to a reduced diffusion length or an enhanced nucleation at defect sites within the oxide monolayer, both being consistent with the STM data. Additionally, decoration of upper and lower step edges (E) can be observed, again. In particular, the islands on the upper edges avoid growing over the step at the third monolayer. Regarding the shape, the islands of the second monolayer are more compact with parts of the step edges aligned in the $[01-1]$ directions. After deposition of 1.1 ML (1050 s), the first monolayer is nearly completely covering the substrate. A layerlike growth proceeds in the second monolayer.

At 1.4 ML, a large number of small islands start to grow in the third monolayer (F) before the second monolayer is completed, indicating the transition to a multilayer growth mode. The nucleation density rises to $1/40\ \text{nm}^2$. Due to the small size of the third monolayer islands, a detailed analysis regarding shape and morphology is difficult from the data presented in Fig. 1.

A more quantitative analysis of the layer-dependent coverage has been obtained by measuring the surface areas of uncovered Pt(111), the monolayer as well as bi- and trilayers in STM images. The coverages were evaluated by dividing the image in Fig. 1 into 33 nm wide horizontal stripes and calculating the respective areas from a histogram. The results are presented in Fig. 2(a). The coverage is displayed for 1 ML (open circles), 2 ML (open triangles), and 3 ML (open diamond) islands as a function of deposition time. Additionally, the coverages of the different layers have been summed up (filled circles). The error on the relative areas due to image resolution and tip geometry has been estimated to be below 1%. Slight image distortions due to thermal drift have been neglected, since a continuous shift would affect all areas in a proportional way and, consequently, cancel out in the area ratio. The uptake curves in Fig. 2 show accurately the coverages for the onset of nucleation and layer completion. In particular, nucleation of 1, 2, and 3 ML starts at MnO coverages of 0, 0.6, and 1.2, respectively, with an estimated error of 0.1. The first monolayer is completed after deposition of 1.1 ML. The increase of the total area (sum curve) represents a linear behavior with deposition time. Slight deviations may originate from systematic errors during analysis of very small (<10 nm) or very frizzy islands. Since a constant Mn atom flux ($\pm 10\%$) was maintained, the number of Mn atoms impinging per unit time and surface area should be constant. With the assumption that the Mn amount (Mn-O stoichiometry) in each layer stays nearly constant, we can conclude that a pronounced loss of Mn at the initial stages of growth due to diffusion into the bulk of the Pt(111) crystal does not take place. This is in agreement with earlier investigations in which bulk alloy formation has been found only at temperatures above 750 K.[24,25] Although an intermixing of Mn and Pt within the first layers of the surface at 400 K

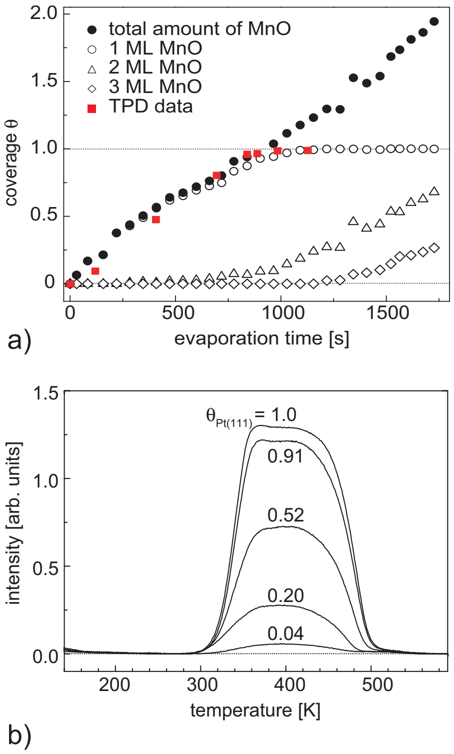

FIG. 2. (Color online) (a) Layer-resolved MnO coverage and remaining bare Pt(111) area as a function of evaporation time during MnO growth. The remaining Pt(111) areas (solid squares) have been calculated from TPD data shown below. (b) TPD spectra (mass: 28 amu) for CO adsorption on the Pt(111) surface which is partially covered by MnO. Since no CO adsorption is found on MnO, the MnO coverages can be extracted from the reduced area for CO adsorption.

could not be excluded in previous studies,[26] we do not observe any indication of embedded MnO layers in the case of Pt(111). This is in contrast to investigations of MnO, CoO, and NiO submonolayer coverages on Ag(001), where embedding of oxide islands has been frequently observed.[27] Here, the different mobilities of the Pt(111) and Ag(001) substrate atoms may play a major role.[22]

As an alternative approach for the MnO coverage determination in the submonolayer regime, titration experiments with CO have been carried out. For this purpose, CO TPD has been performed after exposure of the oxide layer to about 300 L CO at sample temperatures of 80–90 K for different MnO submonolayer coverages. The CO desorption spectra for increasing MnO coverages on Pt(111) are shown in Fig. 2(b) from top to bottom. The clean Pt(111) surface [$\theta_{\mathrm{Pt}(111)}=1$ and $\theta_{\mathrm{MnO}}=0$)] exhibits the typical TPD features known for CO saturation coverage.[28] In particular, a pronounced shoulder at 360 K is indicative for a compressed CO monolayer after increased CO exposure (>50 L at 100 K).[29] In contrast to adsorption on the bare Pt(111) substrate, CO adsorption will not take place on a MnO monolayer. Consequently, the CO TPD intensity decreases linearly with increasing MnO coverage, whereas the overall shape of the desorption spectrum is nearly unaffected. Assuming that the CO adsorbate density on the free Pt(111) regions stays nearly constant, independent of the varying MnO coverage, the amount of CO is directly proportional to the relative area of uncovered Pt(111) $\theta_{\mathrm{Pt}(111)}$. The dependence $1-\theta_{\mathrm{Pt}(111)}$ from the TPD data as function of the Mn evaporation time is plotted in Fig. 2(a) as filled squares. The linear increase of the TPD data with time is clearly visible and agrees well with the STM data after normalizing the evaporation time intervals from the different experimental setups. The approach to 1 for the displayed $1-\theta_{\mathrm{Pt}(111)}$ data clearly indicates the completion of the first MnO monolayer. At MnO coverages beyond 1 ML, CO will not adsorb, which leads to absence of CO in the TPD spectra. This behavior indicates a remarkable inertness of MnO films (>1 ML). For example, the MnO covered Pt(111) surface could be studied in UHV over a time interval of several weeks at elevated temperature (>400 K) without any traces of adsorbates such as, e.g., CO, H_2O, or OH^-.

B. Morphology and atomic structure

The morphology and atomic surface structure of a 1.1 ML thick MnO film is shown in a STM overview image in Fig. 3(a). Besides a step edge in the upper part of the image, clearly holes (H) and islands (I) can be distinguished. Since the main part of the surface is covered by a monolayer, the holes and islands correspond to uncovered Pt(111) and the second MnO layer, respectively. The monolayer regions exhibit a characteristic uniaxial row structure which exists in three rotational domains aligned along the three equivalent high symmetry [01−1] directions. Two of them are marked as D_1 and D_2 in Fig. 3(a). For a monolayer deposited at 400 K, a large number of domains with a size of 30–50 nm is found. Subsequent annealing up to 750 K as shown in Fig. 3(b) leads to an enhanced long-range ordering with larger domains (100 nm). Additionally, areas (D_M) can be identified in Fig. 3(a) where the orientation of the reconstruction rows deviates from the close-packed Pt(111) directions and a small angle of 9°–10° in between is formed. In these regions, a small height modulation may be observed with a slightly varying, long-range periodicity (2.8×1.8 nm^2) and rectangular symmetry as marked by a black rectangle on the upper terrace in Fig. 3(a). It should be noted that these tilted rows are predominantly found between parallel oriented domains and at defects [marked A in Fig. 3(a)]. In some cases (B), they can be regarded as a kind of extended domain boundary, compensating the registry shift between parallel domains. In contrast, sharp domain boundaries (C) are found between 120° rotated domains. Upon annealing to 650 K, the domains oriented in the high-symmetry direction grow on the expense of the small-angle rotated ones as can be seen from Fig. 3(b).

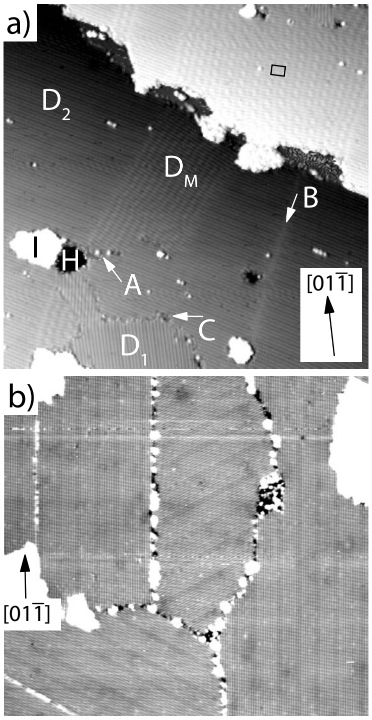

FIG. 3. (a) STM image of 1.1 ML of MnO on Pt(111) at 400 K (70×70 nm^2, $U=-2$ V, $I=0.14$ nA, and $T_{\mathrm{sample}}=400$ K). Different structures are labeled: domains of the monolayer reconstruction (D_1, D_2, D_M), structures at the domain boundaries (A, B, C), 2 ML MnO islands (I), and the Pt(111) substrate (H). (b) STM image of similar MnO coverage after annealing to 670 K, measured at 400 K (100×94 nm^2, $U=1.0$ V, and $I=0.2$ nA).

A typical LEED pattern of the Pt(111) surface with 1 ML MnO is reproduced in Fig. 4. The spots of the Pt(111) substrate unit cell are marked with crosses. Along the main lattice directions, several superstructure spots are observed, which we attribute to the uniaxial reconstruction of the MnO monolayer. In agreement with the large domain size present after deposition at 400 K and annealing to temperatures of 500 K and higher, we find sharp superstructure spots with a high signal-to-background ratio. All of these spots can be well explained by a superposition of the uniaxial superstruc-

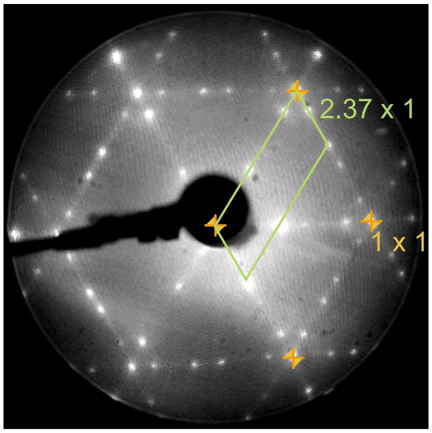

FIG. 4. (Color online) LEED pattern of 1 ML MnO on Pt(111) showing the Pt(111)-(1×1) bulk lattice (crosses) and (19×1) superstructure spots (E_0=80 eV).

ture cell drawn in Fig. 4 in threefold rotational and mirror symmetry. A first order commensurate superstructure may be excluded due to the asymmetric arrangement of the superstructure spots around the first order beam of the Pt(111) substrate. The periodicity of the uniaxial reconstruction rows has been determined with reference to the Pt(111) unit cell. Since the LEED pattern exhibits a slight distortion caused by magnetic stray fields, the relative spot distances have been measured and calculated locally and averaged for the different domains. Within the limits of accuracy, we obtain a (2.37×1) periodicity.

The 2.37-fold periodicity agrees well with the averaged row distance of 0.66 nm measured in STM data displayed in Fig. 5(a). Here, two differently oriented domains are shown at high resolution. At the domain boundary, various imperfections are localized. Close to the island (I), an area (D_M) with a small-angle (δ=10°) rotated row structure can be identified. Such rotated row structures can separate small domains from larger parallel ones as seen in Fig. 5(a). At different locations, various point defects may be identified. A particular type of point defect (marked P in Fig. 5) which appears as a slight depression on top of reconstruction rows was used as marker in subsequent experiments. The profile in Fig. 5(b) was measured along the line (L) in Fig. 5(a). Besides the row structure with the 2.37-fold periodicity, deeper grooves can be distinguished which split the mounds in groups of 3 and 2. These triple and double rows appear in all domains as visible in Fig. 5(a) for two domains. An analysis of several STM images with large, defect-free domains yields a predominant 2-3-3 sequence (>67% of all rows). However, at some locations, an imperfect sequence of triple and double rows can be observed as is visible in Fig. 5(a) close to a defect (P), e.g., a 2-3-2 sequence of double and triple rows.

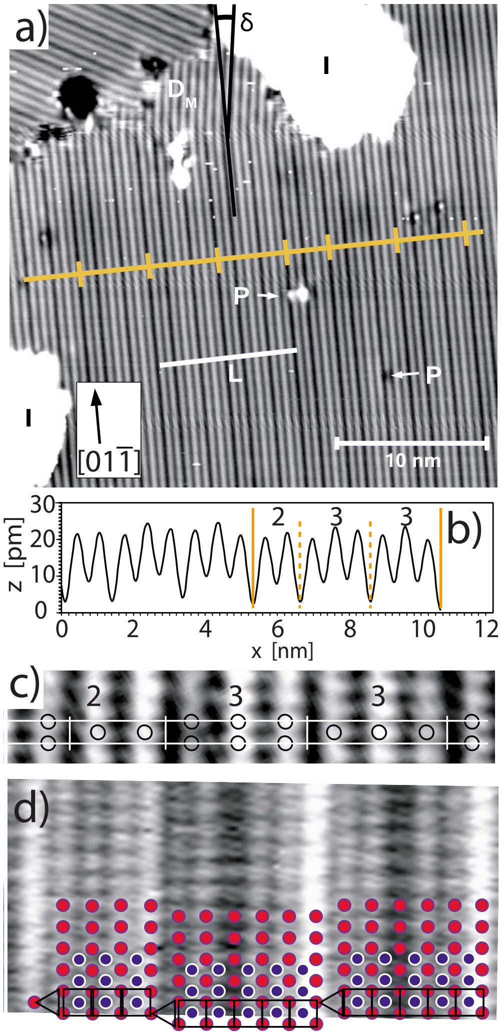

FIG. 5. (Color online) High-resolution STM images of the MnO monolayer on Pt(111): (a) (19×1) domains with profile line (b) along L (32×33 nm^2, U=−2 V, I=0.14 nA, and T_{sample}=400 K). (c) Atomic corrugation of the (19×1) structure (4.9×0.9 nm^2, U=−0.01 V, I=20 nA, and T_{sample}=400 K). (d) Atomically resolved STM image of the MnO-(19×1) monolayer with proposed structure model in the lower part (5.7×2.9 nm^2, U=−0.1 V, I=2 nA, and T_{sample}=300 K).

High-resolution STM images of such 2-3-3 sequences are shown in Figs. 5(c) and 5(d). The uniaxial rows of the reconstruction are clearly visible in Fig. 5(c) with a corrugation of 20 pm. The position of the deeper grooves has been determined from a larger scan as shown in Fig. 5(a) and marked by short vertical line segments. Along the [01−1]-oriented rows, an atomic corrugation with substrate unit cell periodicity and a height of 10 pm can be determined [Fig. 5(c)]. Closer inspection of the atomic periodicity yields a registry shift in [01−1] direction between triple and double row groups. The position of the visible protrusions has been marked by open circles in Fig. 5(c). A phase shift close to half a unit cell in [01−1] direction occurs at the grooves with reference to the white horizontal line running in [−211] direction. Furthermore, a slight buckling is observed perpendicular to the rows, leading to an increased apparent height of the central row within the triple groups.

Figure 5(d) shows the atomic structure of the MnO monolayer highly resolved with different contrast due to different tunneling conditions. Whereas in Fig. 5(c) and in all large area images every *second* atomic row is imaged as protru-

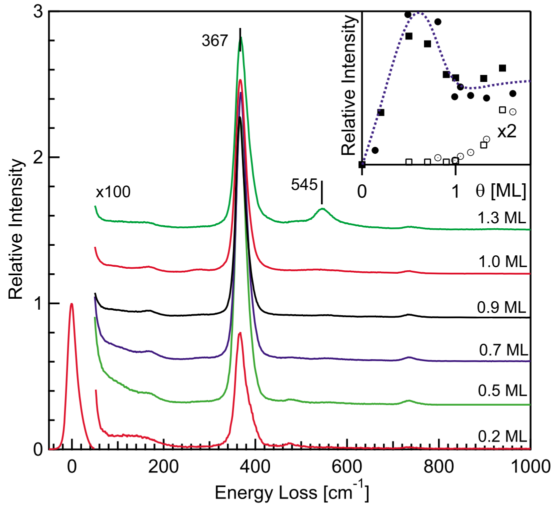

FIG. 6. (Color online) HREEL spectra of MnO layers on Pt(111) for various coverages between 0.2 and 1.3 ML. All layers have been annealed to 650 K. The inset shows the intensities of the 367 and 545 cm^{-1} losses relative to the specular beam intensity as function of MnO coverage. Spectra were recorded with 4 eV electron energy in specular direction.

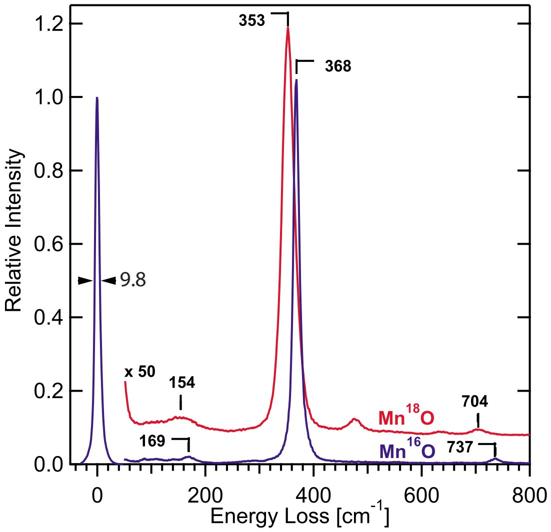

FIG. 7. (Color online) HREEL spectra of isotopically labeled Mn^{16}O and Mn^{18}O monolayers on Pt(111). Both spectra were recorded with 4 eV electron energy in specular direction. Note the different experimental resolutions used.

sion, in Fig. 5(d) all atoms of one sublattice are resolved. The high-resolution image clearly displays a local quadratic structure within each double and triple row stripe. Between the stripes, a registry shift in $[01-1]$ direction by half a unit cell is observed for the quadratic structures. This leads to a triangular arrangement between the stripes. The proposed structural model which will be discussed below is sketched in the lower part of Fig. 5(d). Note that only one sublattice, e.g., only the Mn atoms, is imaged under typical tunneling conditions.

C. Vibrational properties

Vibrational spectroscopy has been applied for the spectroscopic characterization of the oxide layer upon reactive Mn evaporation in an oxygen atmosphere of $(5-6)\times 10^{-8}$ mbar. The substrate temperature during deposition was 375 K, followed by annealing to 650 K under UHV. Figure 6 shows six different HREEL spectra for manganese oxide layers with (bottom to top) increasing Mn evaporation times. The oxide coverage is indicated on the right side of Fig. 6. It has been determined by the amount of desorbing CO in TPD experiments upon CO adsorption at 80 K in comparison to CO desorption from the bare Pt(111) surface [as shown in Fig. 2(b)]. The HREEL spectra are characterized by a strong phonon peak at 364–368 cm^{-1} and a weak and broad feature at about 100–170 cm^{-1}. Both energy losses are absent on the bare Pt(111) surface. The dominant phonon mode at 367 cm^{-1} is attributed to the collective vertical vibration of the oxygen sublattice against the Mn sublattice. For thicker oxide layers, this mode would correspond to the optical Fuchs-Kliewer phonon,[30] which has been found at approximately 572 cm^{-1} in the case of MnO(100).[31] However, in the monolayer, the dipole-active phonon mode is strongly red-shifted due to the interaction with the substrate. Interestingly, this mode is already well developed from 0.2 ML and its frequency stays constant within 4 cm^{-1} up to 1 ML. Its intensity normalized to the elastic peak grows linear with coverage up to 0.5 ML, as shown of the inset of Fig. 6. For higher coverages up to 1 ML the intensity drops and stays constant above. The broad loss features in the 100–170 cm^{-1} range are assigned to acoustic modes and vibrations parallel to the surface due to their low frequencies and weak intensities. For coverages above 1 ML, an additional energy loss at 545 cm^{-1} (see Fig. 6 for 1.3 ML) is observed, which is assigned to the "Fuchs-Kliewer phonon" of the oxide bilayer. Its relative intensity grows as shown in the inset of Fig. 6 (open symbols) with the appearance of the second layer. Note that the energy loss of 545 cm^{-1} is already close to the frequency of the Fuchs-Kliewer phonon for MnO(100). The weak feature at about 735 cm^{-1} visible in all spectra is due to the double excitation of the 367 cm^{-1} phonon. A weak peak at about 480 cm^{-1} in the 0.2 and 0.5 ML spectra is due to the small amount of CO adsorbed on the uncovered Pt(111) surface. Spectra taken without initial annealing to 650 K (not shown here) exhibit similar vibrational features. However, due to the reduced long-range order, the energy loss peaks are broadened. Figure 7 shows a comparison of the monolayer spectrum upon preparation with the different oxygen isotopes ^{16}O and ^{18}O. The manganese ^{16}O spectrum has been recorded with a higher resolution of 9.8 cm^{-1} (1.2 meV) here. Due to the higher resolution, the position of the optical phonon can be accurately determined to 368 cm^{-1}. The width of the phonon peak of 13.2 cm^{-1} yields an intrinsic phonon width of 8.8 cm^{-1} after deconvolution with the instrumental resolution. This narrow width indicates a well-ordered oxide structure. For the ^{18}O-substituted layer, the optical phonon loss is 15 cm^{-1} redshifted to 353 cm^{-1} as shown in Fig. 7, which corresponds to an isotopic ratio of 1.042. This ratio is close to the theoretical value of 1.046, which is given by the

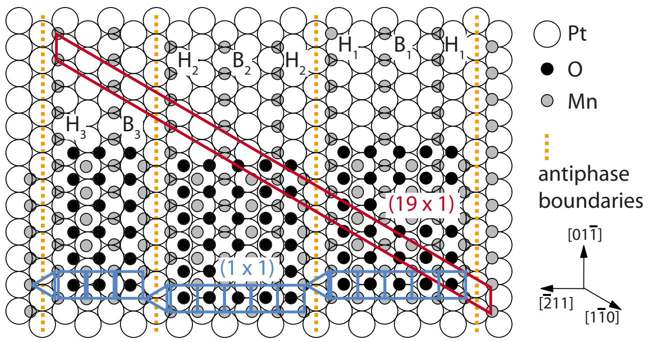

FIG. 8. (Color online) Structure model for the MnO monolayer on Pt(111): The dominant MnO(001)-(1×1)-like building blocks are indicated by squares. Triangular atomic arrangements occur at antiphase boundaries between MnO(001)-like triple and double rows. The total (19×1) unit cell on Pt(111) is indicated. Hollow (H_x) and bridge site (B_x) adsorption in the three different MnO(001)-like areas within the (19×1) unit cell are labeled.

square root of the ratio of the reduced masses for a vibration of the oxygen against the manganese sublattices.

IV. DISCUSSION

The monolayer coverage of MnO on Pt(111) is characterized by the layerlike growth of large domains with a uniaxial reconstruction and nearly defect-free long-range ordering. The long-range order upon annealing to 650 K results in a single remarkably narrow phonon peak. For a better understanding of the atomic arrangement and its interplay with monolayer growth, we put forward a simple model. It contains the main structural properties as they have been deduced from STM, LEED, and HREELS measurements. A schematic drawing of the proposed MnO monolayer is displayed in Fig. 8.

We conclude from the uniaxiality of the reconstruction that the atomic positions within the rows follow the periodicity of the substrate pseudomorphically in [01−1] direction. The rational value of the interrow distance (2.37 substrate unit cells) as determined from LEED patterns would imply a higher-order commensurability of the overlayer lattice in the [−211] direction. However, a distinction from an incommensurate periodicity characterized by an irrational number[32] is not possible on the basis of the obtained LEED data. Further information may be drawn from STM measurements [Fig. 5(a) and 5(b)]. In particular, the ordering of triple and double rows leads to the assumption that the value of 2.37 results from averaging of various interrow periodicities between 2.3 and 2.4. The regular arrangement of the 2-3-3 sequence is induced by the finite interaction energy in the overlayer-substrate system. Based on the description of the overlayer lattice by rational numbers in both [01−1] and [−211] directions, we assume a higher-order commensurate coincidence lattice.

The registry shift of half a unit cell which has been experimentally observed between triple and double rows, the predominant 2-3-3 sequence, and the approximately quadratic structure between the antiphase boundaries as observed in Fig. 5(d) can unambiguously be reproduced by the model in Fig. 8. One-half of one atomic species of the oxide, e.g., the Mn atoms, occupies preferentially high-symmetry, hollow (H_{1-3}) and bridge (B_{1-3}) sites. The triple ($H_{1,2},B_{1,2}$) and double (H_3,B_3) arrangements of atoms are aligned to the [−211] direction with a distance of 2.33 substrate unit cells. In [01−1] direction, a pseudomorphic unit cell periodicity is maintained, yielding the uniaxial reconstruction rows. Between the triple rows, a row distance of 2.33 substrate unit cells and a 180° registry shift are located due to the substrate symmetry. In a similar way, the double rows are arranged with a 180° phase shift with row distances of 2.33 and 2.66 substrate unit cells, respectively. The resulting 2-3-3 sequence is made up of eight reconstruction rows distributed over 19 ($19=7\times2.33+1\times2.66$) close-packed substrate rows. The resulting average row distance of $19/8=2.375$ substrate unit cells agrees well with the value of 2.37 obtained from LEED data. The superstructure unit cell of the 2-3-3 sequence can be described as a (19×1) mesh with a multiatomic basis. In particular, the triple atom arrangements constitute identical subunits which can be interpreted as small, approximately quadratic domains with a periodicity of (2.33×1), a width of 7 substrate unit cells, and intermediate antiphase boundary. Note that the 2-3-3 sequence can be easily disturbed by surface inhomogeneities such as, e.g., defects: Figure 5(a) shows from left to right six 2-3-3 sequenced unit cells and one sequence fault close to a defect. In larger scale STM images as in Fig. 3(b), the 2-3-3 sequence is barely visible as a slightly darker contrast of the double rows. Based on the model in Fig. 8, the LEED pattern is explained in terms of electron diffraction at an ordered (19×1) arrangement of small domains and antiphase boundaries (double and triple rows).[33] A perfectly ordered (19×1) reconstruction would yield 19 sharp fractional order spots along the main crystal axes. In our data, the intensity of these spots is modulated by two form factors arising from the (2.33×1) row periodicity and the (7×1) periodicity of the triple rows in the 2-3-3 sequence. In general, the form factor of a limited number N of scattering units as in small domains shows a broad peak with a full width at half maximum (FWHM) of $1/N$ of the corresponding spot distance in reciprocal space.[33] This yields a nominal FWHM width of the form factor peak for the (2.33×1) triple rows of 7.15% of the first Brillouin zone (BZ). The form factor of the (7×1) periodicity of both triple rows in the 2-3-3 sequence has a FWHM width of 3.57% of the first BZ. As a result, a measurable intensity is only obtained for those (19×1) spots close to the (2.33×1) spots (<3.57% of the first BZ). Since the distance between the sharp (19×1) spots (5.26% of the first BZ) is larger than that region, the LEED pattern shows intensity only for the 8th and the 16th fractional order spots of the (19×1) structure. The position calculated for the 8th fractional order spot is $8/19=1/2.375$, which corresponds to the measured value. For comparison, the diffraction pattern has also been successfully calculated in a simple simulation experiment by applying fast-Fourier transformation to a two-dimensional image of the reconstruction model (not shown here).

Regarding the composition of the monolayer, we expect a stoichiometry close to MnO since (001)-oriented MnO films were obtained on Ag(001) under similar preparation conditions.[14] According to Tasker's rule, the growth of nonpolar (001) layers should be energetically preferred for rock-salt MnO.[11] The vibrational characteristics (as shown in Figs. 6 and 7) of a single, strong, and narrow phonon peak in the MnO monolayer points to a homogenous layer with only one oxygen species. All vertical oxygen vibrations are coupled into this phonon mode. The isotopic ratio for the Mn^{16}O and Mn^{18}O layers can be understood based on the collective vibration of oxygen and manganese sublattices against each other. Such a motion explains also the high intensity of this phonon by a large dynamical dipole moment.

Based on these findings and the highly resolved STM image in Fig. 5(d), we propose an atomic configuration within the (2.33×1) rows similar to a (001)-oriented MnO layer [lower half in Figs. 5(d) and 8]. The rectangular symmetry of the unit cell (marked by open squares) particularly in the center of the triple rows is confirmed by the high-resolution STM measurement in Fig. 5(d). Within the triple row structures, the MnO film is connected to the substrate at the hollow and bridge sites, leading to a misfit of 11.8% in $[0-11]$ direction and 10.6% in $[-211]$ direction. The compressive strain in $[-211]$ direction is followed by a buckling of the MnO overlayer, which adds to the corrugation of the reconstruction rows as seen by STM [Figs. 5(a) and 5(c)].

At the antiphase boundaries, a triangular atomic coordination is proposed in the structure model (Fig. 8). Presuming a pseudomorphic unit cell periodicity in $[0-11]$ direction, several atomic structures seem possible here: (a) missing O rows (as shown in Fig. 8), (b) MnO in a local (111)-like orientation, and (c) O adatom rows leading to a locally higher O coordination of Mn. Whereas the details along the antiphase boundaries cannot be inferred from Fig. 5, depending on the detailed preparation conditions, STM images (not shown here) sometimes show enhanced noise here. This might be interpreted as oxygen vacancy diffusion along the antiphase boundaries.

Whereas the (19×1) periodicity is easily disturbed by defects, the triple and double reconstruction rows represent stable building blocks of the monolayer. Single or four and more rows have never been observed. The observed small-angle rigid rotation of the MnO monolayer which is induced by local defects or domain boundaries (see Fig. 5) indicates that the observed STM contrast of the monolayer is largely due to an intrinsic property of the monolayer rather than due to height modulations simply based on hollow versus on top adsorption sites. For the small-angle rotated structure, the film accommodates to the substrate by formation of weak moiré-like patterns [see domain marked D_M in Fig. 3(a)]. A stronger influence arises from step edges. After annealing, a preferential alignment of the reconstruction rows parallel to the high-symmetry $[01-1]$ directions is found as shown in Fig. 3(b), indicating the energetically favored arrangement.

The atomic structure during growth of the first monolayer at 400 K is kinetically restricted. This can be concluded from the formation of dendritic islands pointing in $[01-1]$ directions. The growth of anisotropic, fractal-dendritic islands observed at lower temperatures (400 K) and submonolayer coverages is known from homoepitaxial studies on many fcc(111) metal surfaces,[34] leading to a preferential orientation of island branches in $[-211]$ direction. As shown in Fig. 1, we also find an anisotropic growth, but the branches of the islands point in the $[01-1]$ directions of the substrate. Almost one-dimensional branches with a very low aspect ratio appear. The latter indicates an interesting analogy to the one-dimensional growth of Ni-O adsorbate structures on Pt(111), where a uniaxial (7×1) reconstruction was observed.[35] The growth phenomenon has been explained by an anisotropic step edge diffusion and step adatom binding probability caused by the particular structural anisotropy of either uniaxially reconstructed islands themselves or an interaction between the islands and the Pt(111) substrate (e.g., substrate lattice distortions). For the uniaxially reconstructed MnO monolayer on Pt(111), a similar interaction of structure and adatom diffusion may determine the growth dynamics.[35] According to the model in Fig. 8, atoms follow pseudomorphically the substrate unit cell periodicity within the reconstruction rows, leading to densely packed step parallel edges. Perpendicular edges yield a more open structure due to buckling and the misfit of the MnO(001)-like row structure along the $[-211]$ direction of the (111) substrate. Accordingly, an increased diffusion along the $[1-10]$ steps and a higher binding probability for adatoms at $[-211]$ steps appear reasonable. As a result, a pronounced diffusion anisotropy is obtained, leading to the observed anisotropic, fractal-dendritic island shape as well as the local formation of one-dimensional islands elongated in $[1-10]$ direction.

V. CONCLUSION

The growth, structural, and vibrational properties of the first MnO monolayer on Pt(111) have been studied using STM, LEED, TPD, and HREELS. Deposition of Mn in O_2 atmosphere between 5×10^{-8} and 2×10^{-7} mbar onto Pt(111) at 400 K leads to a layerlike growth of the first MnO layers. The first MnO monolayer exhibits an almost perfect wetting behavior of the Pt(111) substrate with nucleation of the second monolayer at a total coverage of 0.8 ML. Based on STM and LEED, a commensurate uniaxially reconstructed (19×1) reconstruction of a MnO(100)-like monolayer is found. This monolayer is dominated by an atomic row structure with an approximate $(19/8\times1)$ periodicity. Upon deposition, it forms large well-ordered domains which can be further improved by annealing to 650 K in UHV. The monolayer is characterized by a strong and narrow (9 cm^{-1} FWHM) surface phonon at 368 cm^{-1}, which exhibits a clear ^{16}O-^{18}O isotope shift and corresponds to a collective vertical vibration of all O atoms against the Mn sublattice. We propose a structural model for the (19×1) monolayer, which is based on a nonpolar, (001)-oriented MnO layer. The stress induced by the large lattice mismatch (13%) is relieved by a buckling of the (001) monolayer with a uniaxial $(19/8\times1)$ periodicity and a long-range ordering of antiphase boundaries between double and triple atomic rows. Between the large (19×1) domains, various domain boundaries appear depending on the relative domain orientation. Whereas domains which are rotated by 120° develop sharp common boundaries, parallel domains accommodate their structural mismatch over extended areas, forming typical moiré patterns. At elevated temperatures above 400 K, the surface stays free of adsorbates over time intervals of several weeks, indicating a remarkable chemical inertness at these conditions.

ACKNOWLEDGMENTS

The authors thank H. Neddermeyer for stimulating discussions. Financial support by the Deutsche Forschungsgemeinschaft (DFG) through the Research Group FOR-404 “Oxidic Interfaces” is gratefully acknowledged.

---

*Present address: Fraunhofer-Institut für Werkstoffmechanik, Halle, Germany.

†Permanent address: Institute of General and Inorganic Chemistry, Bulgarian Academy of Sciences, 1113 Sofia, Bulgaria.

‡Corresponding author; wolf.widdra@physik.uni-halle.de

[1] A. R. Armstrong and P. G. Bruce, Nature (London) **381**, 499 (1996).

[2] M. J. Han, T. Ozaki, and J. J. Yu, J. Chem. Phys. **123**, 034306 (2005).

[3] M. Baldi, E. Finocchio, C. Pistarino, and G. Busca, Appl. Catal., A **173**, 61 (1998).

[4] R. J. Lad and V. E. Henrich, Phys. Rev. B **38**, 10860 (1988).

[5] V. E. Henrich and P. A. Cox, *The Surface Science of Metal Oxides* (Cambridge University Press, Cambridge, England, 1993).

[6] J. E. Pask, D. J. Singh, I. I. Mazin, C. S. Hellberg, and J. Kortus, Phys. Rev. B **64**, 024403 (2001).

[7] W. S. Seo, H. H. Jo, K. Lee, B. Kim, S. J. Oh, and J. T. Park, Angew. Chem. **43**, 1115 (2004).

[8] J. Park, E. A. Kang, C. J. Bae, J. G. Park, H. J. Noh, J. Y. Kim, J. H. Park, and T. Hyeon, J. Phys. Chem. B **108**, 13594 (2004).

[9] H. Landoldt and R. Börnstein, *Numerical Data and Functional Relationships in Science and Technology* (Springer, Berlin, 1997).

[10] P. A. Cox, *Transition Metal Oxides* (Oxford University Press, Oxford, 1995).

[11] P. W. Tasker, J. Phys. C **12**, 4977 (1979).

[12] C. Franchini, V. Bayer, R. Podloucky, G. Parteder, S. Surnev, and F. P. Netzer, Phys. Rev. B **73**, 155402 (2006).

[13] V. Bayer, C. Franchini, and R. Podloucky, Phys. Rev. B **75**, 035404 (2007).

[14] F. Müller, R. de Masi, D. Reinicke, P. Steiner, S. Hüfner, and K. Stowe, Surf. Sci. **520**, 158 (2002).

[15] G. A. Rizzi, R. Zanoni, S. Di Siro, L. Perriello, and G. Granozzi, Surf. Sci. **462**, 187 (2000).

[16] W. Neubeck, L. Ranno, M. B. Hunt, C. Vettier, and D. Givord, Appl. Surf. Sci. **139**, 195 (1999).

[17] K. Marre and H. Neddermeyer, Surf. Sci. **287**, 995 (1993).

[18] W. B. Pearson, *Handbook of Lattice Spacings and Structures of Metals and Alloys* (Pergamon, New York, 1958).

[19] K. Meinel, A. Eichler, K.-M. Schindler, and H. Neddermeyer, Surf. Sci. **562**, 204 (2004).

[20] K. Meinel, A. Eichler, S. Förster, K.-M. Schindler, H. Neddermeyer, and W. Widdra, Phys. Rev. B **74**, 235444 (2006).

[21] K. L. Kostov, M. Gsell, P. Jakob, T. Moritz, W. Widdra, and D. Menzel, Surf. Sci. **394**, L138 (1997).

[22] C. Hagendorf, R. Shantyr, and H. Neddermeyer, in *Scanning Tunneling Microscopy/Spectroscopy and Related Techniques: 12th International Conference STM’03*, edited by P. M. Koenraad and M. Kemerink (AIP, New York, 2003), p. 810.

[23] M. B. Hugenschmidt, L. K. Verheij, M. K. Freitag, B. Poelsema, and G. Comsa, Surf. Sci. **259**, L763 (1991).

[24] S. Gallego, C. Ocal, J. Mendez, X. Torrelles, and F. Soria, Surf. Sci. **482**, 1303 (2001).

[25] S. Gallego, C. Ocal, M. C. Munoz, and F. Soria, Phys. Rev. B **56**, 12139 (1997).

[26] M. Scarselli, L. Dragone, A. Sgarlata, M. Fanfoni, V. Di Castro, and R. Zanoni, Surf. Sci. **545**, L774 (2003).

[27] I. Sebastian, T. Bertrams, K. Meinel, and H. Neddermeyer, Faraday Discuss. **114**, 129 (1999).

[28] K. L. Kostov, P. Jakob, and D. Menzel, Surf. Sci. **377-379**, 802 (1997).

[29] H. Steininger, S. Lehwald, and H. Ibach, Surf. Sci. **123**, 1 (1982).

[30] R. Fuchs and K. L. Kliewer, Phys. Rev. **140**, 2076 (1965).

[31] M. A. Langell, C. W. Hutchings, G. A. Carson, and M. H. Nassir, J. Vac. Sci. Technol. A **14**, 1656 (1996).

[32] P. Bak, Rep. Prog. Phys. **45**, 587 (1982).

[33] M. A. Van Hove, W. H. Weinberg, and C.-M. Chan, *Low-Energy Electron Diffraction* (Springer-Verlag, Berlin, 1986).

[34] M. Bott, M. Hohage, T. Michely, and G. Comsa, Phys. Rev. Lett. **70**, 1489 (1993).

[35] C. Hagendorf, R. Shantyr, H. Neddermeyer, and W. Widdra, Phys. Chem. Chem. Phys. **8**, 1575 (2006).